# Hierarchically CdS Decorated 1D ZnO Nanorods-2D Graphene Hybrids: Low Temperature Synthesis and Enhanced Photocatalytic Performance

*Chuang Han, Zhang Chen, Nan Zhang, Juan Carlos Colmenares,* and Yi-Jun Xu**

**A simple, low-temperature synthesis approach is reported for planting CdS-sensitized 1D ZnO nanorod arrays on the 2D graphene (GR) sheet to obtain the ternary hierarchical nanostructures, during which graphene oxide (GO) as the precursor of GR acts as a flexible substrate for the formation of ZnO nanorod arrays. The hierarchical CdS-1D ZnO-2D GR hybrids can serve as an efficient visible-light-driven photocatalyst for selective organic transformations. The fast electron transport of 1D ZnO nanorods, the well-known electronic conductivity of 2D GR, the intense visible-light absorption of CdS, the unique hierarchical structure, and the matched energy levels of CdS, ZnO and GR efficiently boost the photogenerated charge carriers separation and transfer across the interfacial domain of hierarchical CdS-1D ZnO-2D GR hybrids under visible light irradiation via three-level electron transfer process. Furthermore, the superior reusability of ternary hybrids is achieved by controlling the reaction parameters, i.e., using visible light irradiation and holes scavenger to prevent ZnO and CdS from photocorrosion. This work demonstrates a facile way of fabricating hierarchical CdS-1D ZnO-2D GR hybrids in a controlled manner and highlights a promising scope of adopting integrative photosensitization and co-catalyst strategy to design more efficient semiconductor-based composite photocatalysts toward solar energy capture and conversion.**

## 1. Introduction

The eternal pursue for sustainable energy and environment keeps moving, together with kinds of potential challenges existing. A promising project, which can afford us the flexibility to tackle such challenges, lies in designing efficient semiconductor-based photocatalysts for the maximal capture and conversion of solar energy, mimicking the natural photosynthesis process.[1] In this context, targeted engineering of photocatalysts with diverse structure and morphology has been gaining immense attention due to that many microscopic structural and morphology factors (e.g., size, shape, crystal facet, localized compositional variation and heterojunction of the given semiconductor-based materials) have synergistic impacts on the overall performance of photocatalysts.[1,2] Therefore, considering the basic mantra of "structure-dictates-function" in chemistry,[3] it is of paramount importance to design efficient semiconductor-based materials with desirable architectural structure/morphology toward various photoredox applications.[1,2,3b,3c]

In view of high surface-to-volume ratio and excellent electron transport property, one dimensional (1D) nanostructured materials are believed to play an important role in the next-generation building blocks for electronic devices, solar cells, photocatalysis, lithium-ion batteries and piezoelectric nanogenerators.[4] In particular, ZnO nanorod arrays with tunable alignment and morphology have attracted much attention in the field of energy conversion.[5] Despite plenty of reports on the synthesis and application of ZnO nanorod arrays, the reported synthetic procedures often need the conventional case-hardened FTO/$Al_2O_3$/GaN/Si substrates or $SiO_2$/Si, FTO/Si substrates along with high temperature thermal treatment.[5d,5e,6] Thus, it is highly desirable to develop simple, low-cost and low-temperature processes for controllable synthesis of 1D ZnO nanoarrays on alternative substrates. In this regard, 2D graphene would be a favorable choice owing to its excellent electronic conductivity and unique 2D sheet providing a large accessible surface platform.[3b,7] Additionally, from the viewpoint of photocatalysis, due to the wide band gap of semiconductor ZnO (3.2 eV), it only adsorbs ultraviolet light accounting for a small fraction of the solar spectrum (<5%), which greatly obstructs its practical applications.[6a,8] Besides, the other drawback associated with ZnO photocatalyst is the well-known photocorrosion induced by the photogenerated holes, which leads to the poor photostability or deactivation during the long-term recycling use.[9]

Herein, we report a facile low-temperature synthesis of planting CdS-sensitized 1D ZnO nanorod arrays on the 2D graphene sheet via a heteroepitaxial growth process in a solution phase. The as-obtained hierarchically CdS decorated 1D

C. Han, Z. Chen, N. Zhang, Prof. Y.-J. Xu
State Key Laboratory of Photocatalysis on Energy and Environment
College of Chemistry, Fuzhou University
Fuzhou, 350002, P. R. China & College of Chemistry
New Campus, Fuzhou University
Fuzhou 350108, P. R. China
E-mail: yjxu@fzu.edu.cn
Prof. J. C. Colmenares
Institute of Physical Chemistry
Polish Academy of Sciences, ul. Kasprzaka 44/52
01–224, Warsaw, Poland
E-mail: jcarloscolmenares@ichf.edu.pl

**DOI: 10.1002/adfm.201402443**

ZnO nanorods-2D graphene hybrids show enhanced photocatalytic activity and excellent recycling performance toward selective reduction process under visible light irradiation. The fast electron transport of 1D ZnO nanorods, the well-known electronic conductivity of 2D graphene, the intense visible-light absorption of CdS, and their matched energy level position together efficiently promote the photogenerated charge carriers separation and transfer across the interfacial domain, thereby resulting in the significantly improved visible-light-driven photocatalytic activity of ternary CdS-1D ZnO-2D GR hybrids as compared to the blank ZnO, binary ZnO nanorods-GR and ZnO nanorods-CdS. Furthermore, because ZnO cannot be band-gap-photoexcited to produce holes under visible light irradiation and the holes photogenerated from CdS are effectively trapped by the scavenger ammonium formate, the photocorrosion of ZnO and CdS can be prevented effectively. Consequently, the CdS-1D ZnO-2D GR hybrids are able to show excellent recycling photocatalytic performance toward selective photogenerated-electrons-driven reduction process. This work provides a simple wet chemical fabrication of hierarchical CdS-1D ZnO-2D GR hybrids in pursuit of the desirable visible-light absorption of CdS and the electron conductive platform of 2D graphene as photosensitizer and co-catalyst respectively to improve the photocatalytic performance by boosting charge carriers separation and transfer efficiency.

## 2. Results and Discussion

Our controlled synthesis of ternary graphene-ZnO nanorod arrays-CdS (denoted as RGO-ZnO NRs-CdS) hybrids by a simple solution bottom-up strategy is illustrated in **Scheme 1**. Firstly, graphene oxide (GO) sheets (the precursor of graphene) are coated with ZnO seeds via a surface adsorption process. Then the obtained ZnO seeds-coated GO sheets are used as the substrate for heteroepitaxial growth of 1D ZnO nanorods to form hierarchical graphene-ZnO nanorod arrays (RGO-ZnO NRs) heteroassemblies. Subsequently, the RGO-ZnO NRs are utilized as the template for morphology-preserved nanocoating of CdS nanoparticles on RGO-ZnO NRs via secondary nucleation and growth procedures. As a result, the RGO-ZnO NRs-CdS hybrids are obtained via such a facile two-step low temperature (95 °C) refluxing method. During this two-step refluxing process for synthesis of RGO-ZnO NRs-CdS, the efficient reduction of GO to RGO can be achieved, as evidenced by the XPS analysis in Figure S1 (Supporting Information). For the synthesis of blank ZnO nanostars and ZnO nanostars-CdS, the synthesis procedures are similar respectively to those for RGO-ZnO NRs and RGO-ZnO NRs-CdS nanocomposites except the addition of colloidal GO.

The morphological evolution process of the RGO-ZnO NRs heteroassemblies has been investigated via time-dependent experiments. As shown by the scanning electron microscopy (SEM) analysis on the RGO-ZnO NRs samples synthesized with different reaction time in **Figure 1**, the ZnO nanorods gradually grow on the RGO sheet during the refluxing process. More specifically, with the refluxing time of 0.5 h, the ZnO nanorods are formed sparsely on the surface of RGO and the uncovered RGO sheet can be clearly seen, as indicated by the arrow in Figure 1A. As the refluxing time increases, the ZnO nanorods planted sideways on the RGO substrate turn from slightly scattered to thickly dotted. For the RGO-ZnO NRs samples prepared with short reaction time (i.e., no more than 2 h), the presence of RGO sheets is distinct (Figure 1A-D). When the refluxing time is prolonged to 3 h, the surface of RGO substrate is almost planted with ZnO nanorods, as shown in Figure 1E. After refluxing for 6 h, the hedgehog-like RGO-ZnO NRs heteroassemblies are obtained, as revealed by the SEM images in Figure 1F, **Figure 2**E and 2F. The unique features of 2D GO sheets with abundant oxygen-containing functional groups (Figure S1A, Supporting Information) make GO be an alternative substrate for the heteroepitaxial growth of 1D ZnO nanorod arrays. In the absence of GO, the blank ZnO nanorods have the star-like morphology, as displayed in Figure 2A and 2B. Thus, the growth and self-assembly of 1D ZnO nanorods are tuned by the colloidal GO in solution. In other words, GO provides a 2D structure-directing platform for anchoring ZnO seeds and the subsequent growth of ZnO nanorod arrays. As for the binary ZnO nanostars-CdS (Figure 2C and 2D) and hierarchical ternary RGO-ZnO NRs-CdS hybrids (Figure 2G and 2H) achieved

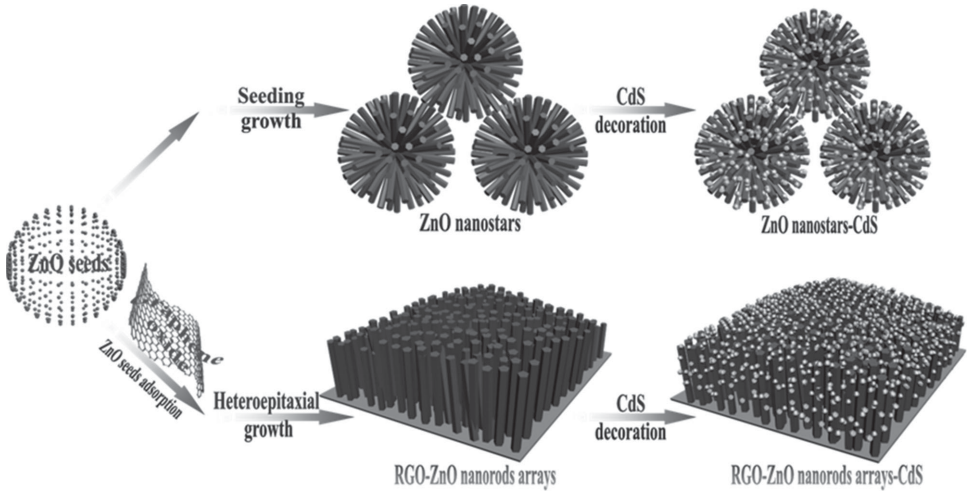


**Scheme 1.** Schematic illustration of controllable synthesis of the hybrids of binary ZnO nanostars-CdS and ternary RGO-ZnO NRs-CdS.

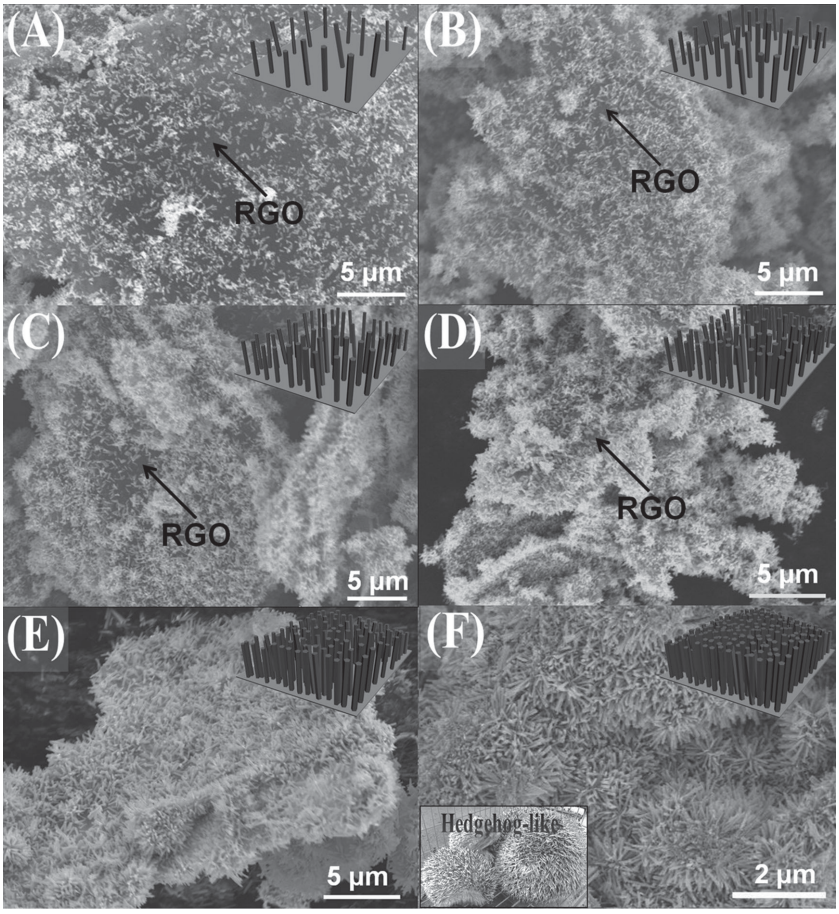


**Figure 1.** SEM images of the ZnO nanorods grown on the RGO platform prepared from 0.02 M $Zn(NO_3)_2$ and 0.02 M HMT at 95 °C for different refluxing time: A) 0.5 h; B) 1 h; C) 1.5 h; D) 2 h; E) 3 h; F) 6 h.

by the decoration of CdS for ZnO nanostars and RGO-ZnO NRs, respectively, the CdS nanoparticles on the surface of 1D ZnO NRs can be obviously observed.

To further obtain the microscopic morphology and structure information, the transmission electron microscopy (TEM) analysis of 5%RGO-ZnO NRs and 5%RGO-ZnO NRs-CdS has been performed, as shown in **Figure 3**. The TEM images of 5%RGO-ZnO NRs (Figure 3A) and 5%RGO-ZnO NRs-CdS (Figure 3B and 3D) show the specific hedgehog-like morphology, which is in accordance with SEM results. The CdS nanoparticles, 1D ZnO NRs and 2D mat of RGO sheets can be clearly distinguished in the TEM images of 5%RGO-ZnO NRs-CdS, as indicated in Figure 3B and 3D. The corresponding EDX spectrum for selected area of 5%RGO-ZnO NRs-CdS, as shown in Figure 3C, confirms the elementary composition of the ternary 5%RGO-ZnO NRs-CdS architecture, which contains C, Zn, O, Cd and S elements. Notably, the lacey support film without carbon coating is used, and thus the signal of C must come from the RGO sheet in the nanocomposite. Indeed, the identification of CdS, ZnO and RGO in 5%RGO-ZnO NRs-CdS can also be distinctly revealed by the following Raman spectroscopy analysis.

Raman spectroscopy, being very sensitive response to the crystallinity and microstructure of materials, is usually used to distinguish the local order character of the nanomaterials.[10] As displayed in Figure S2 (Supporting Information), the Raman spectrum of blank ZnO nanostars shows a Raman shift peak at 437 $cm^{-1}$, which is ascribed to the remarkable $E_{2H}$ mode of hexagonal wurtzite ZnO.[11] In the Raman spectrum of binary 5%RGO-ZnO NRs, the typical features of RGO with the presence of D band located at 1340 $cm^{-1}$ and G band at 1581 $cm^{-1}$ are observed.[12] G band provides the information on the in-plane vibration of $sp^2$ bonded carbon atoms, while the D band is attributed to the presence of $sp^3$ defects in graphene.[3b,13] With regard to the ZnO nanostars-CdS composite, the resonantly excited longitudinal optical (LO) phonon of CdS locates at approximately 300 $cm^{-1}$, together with resonant excitation which allows identifying the first (2 LO) overtone of the CdS at 604 $cm^{-1}$.[14] This demonstrates that the CdS decoration has been successfully realized by our simple low temperature refluxing method. The Raman spectrum of the ternary 5%RGO-ZnO NRs-CdS hybrid exhibits characteristic peaks of RGO and CdS. No evident Raman peak of ZnO can be observed in the ZnO nanostars-CdS, 5%RGO-ZnO NRs and 5%RGO-ZnO NRs-CdS nanocomposites, which is probably due to relatively weak intensity of ZnO in these composites samples. Therefore, the Raman results provide further evidences for the formation of binary RGO-ZnO NRs, ZnO nanostars-CdS and ternary RGO-ZnO NRs-CdS hybrids.

X-ray diffraction (XRD) analysis has been employed for analyzing the crystalline phase of samples, as shown in Figure S3 (Supporting Information). The RGO-ZnO NRs nanocomposites show similar XRD patterns to the pure ZnO nanostars. The main peaks at $2\theta$ values of 31.8, 34.4, 36.3, 47.5, 56.6, 62.9, 68.0° can be respectively indexed to (100), (002), (101), (102), (110), (103), and (112) crystal planes, which can be readily indexed to the pure hexagonal phase ZnO (JCPDS No. 36–1451). After the decoration of CdS nanoparticles onto ZnO nanostars and RGO-ZnO NRs, some additional diffraction peaks corresponding to the hexagonally structured CdS phase (JCPDS No. 41–1049) appear, revealing that ZnO nanostars-CdS and RGO-ZnO NRs-CdS nanocomposites are obtained during the aqueous-phase refluxing process under the premise of heterogeneous nucleation. Furthermore, no diffraction peaks for RGO can be observed in the nanocomposites of RGO-ZnO NRs and RGO-ZnO NRs-CdS, which might be due to the low amount and relatively weak diffraction intensity of RGO in the nanocomposites.[1d,3b,9a,15]

**Figure 4** shows the UV–Vis diffuse reflectance spectra (DRS) of the samples, which reflect the optical properties of the materials in different wavelength range. It is seen from Figure 4A that the introduction of different weight contents of RGO has

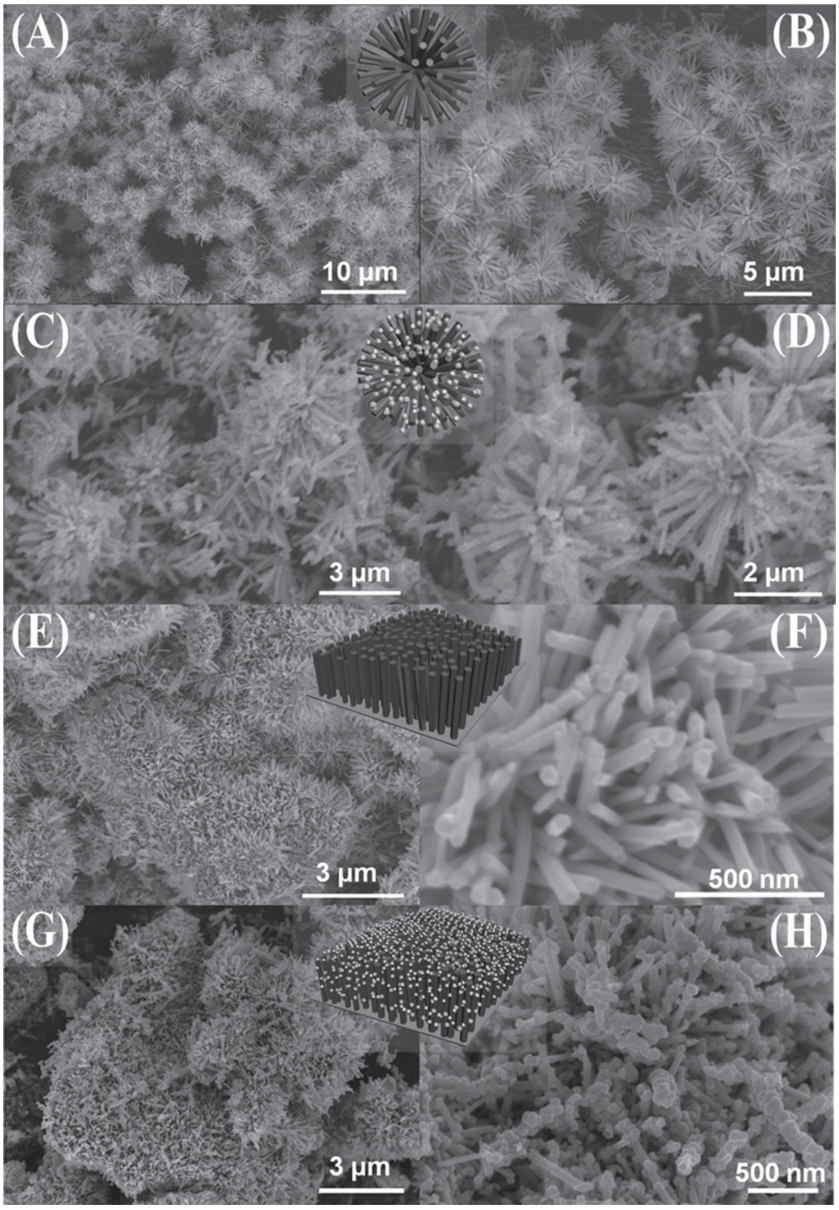


**Figure 2.** SEM images of A, B) ZnO nanostars, C, D) ZnO nanostars-CdS, E, F) binary 5%RGO-ZnO NRs and G, H) ternary 5%RGO-ZnO NRs-CdS hybrids.

a significant effect on the optical light absorption property for the RGO-ZnO NRs nanocomposites. With the increase of RGO content, there is an enhanced absorbance in the visible light region ranging from 400 to 800 nm. Nevertheless, the optical absorption edge of RGO-ZnO NRs is similar to that of bare ZnO nanostars, indicating that both RGO-ZnO NRs and bare ZnO nanostars can be only band-gap-photoexcited by UV light irradiation. As shown in Figure 4B, after the CdS decoration onto RGO-ZnO NRs and ZnO nanostars, a new optical absorption edge appears which is characteristic of semiconductor CdS. As a result, both ZnO nanostars-CdS and RGO-ZnO NRs-CdS nanohybrids are able to be band-gap-photoexcited by visible light irradiation, by which photocatalytic target reactions could be triggered.

We have then investigated the photocatalytic performance of these samples toward anaerobic reduction of aromatic nitro compounds to corresponding amino compounds in water, a key transformation in synthesis of fine chemicals,[3c,16] which can be expressed by the formula shown in **Figure 5**A. Figure 5B and 5C show the photocatalytic activities of the as-prepared samples toward selective reduction of 4-nitroaniline (4-NA) to *p*-phenylenediamine (PPD) under visible light irradiation. It is seen that the RGO-ZnO NRs-CdS nanocomposites exhibit enhanced photocatalytic performance as compared to ZnO nanostars, RGO-ZnO NRs and ZnO nanostars-CdS. In particular, the 5%RGO-ZnO NRs-CdS exhibits the best photocatalytic activity. After reaction for 16 min under visible light irradiation, the conversion of 4-NA reaches as high as 95% with a high selectivity for PPD (>98%) over 5%RGO-ZnO NRs-CdS (Figure S4, Supporting Information). The photostability of the RGO-ZnO NRs-CdS hybrids has also been studied. As shown in Figure S5 (Supporting Information), no significant loss of photoactivity is observed for 5%RGO-ZnO NRs-CdS during four successive recycling test for reduction of 4-NA under visible light irradiation. Through comparing the crystalline phase and morphology of the fresh and used 5%RGO-ZnO NRs-CdS (Figure S6 and S7, respectively in the Supporting Information), it can be found that there is no obvious change in the crystalline phase and morphology of 5%RGO-ZnO NRs-CdS after the photocatalytic process, which is in line with its remarkable repeated photoactivity. Thus, the photocorrosion of ZnO and CdS can be efficiently prevented by controlling the reaction conditions to exclude the formation of holes in ZnO and consume the holes photogenerated from CdS through using visible light illumination and holes scavenger ammonium formate, respectively, thus leading to the excellent photostability of RGO-ZnO NRs-CdS hybrids.

Similar enhancement of photocatalytic activity is also found in selective reduction of other aromatic nitro compounds with various substituent groups over ZnO nanostars-CdS and 5%RGO-ZnO NRs-CdS, as shown in Figure S8A-F (Supporting Information). Since the photocatalytic reduction efficiency is intimately related with the fate and transfer of photogenerated electrons,[17] such a photoactivity enhancement for the ternary 5%RGO-ZnO NRs-CdS hybrid should be attributed to improved charge carriers transport and synergistic interactions among RGO, semiconductor CdS and ZnO. The inference can be evidenced by the following photoelectrochemical and photoluminescence characterization of the optimal 5%RGO-ZnO NRs-CdS, ZnO nanostars-CdS composite and bare ZnO nanostars.

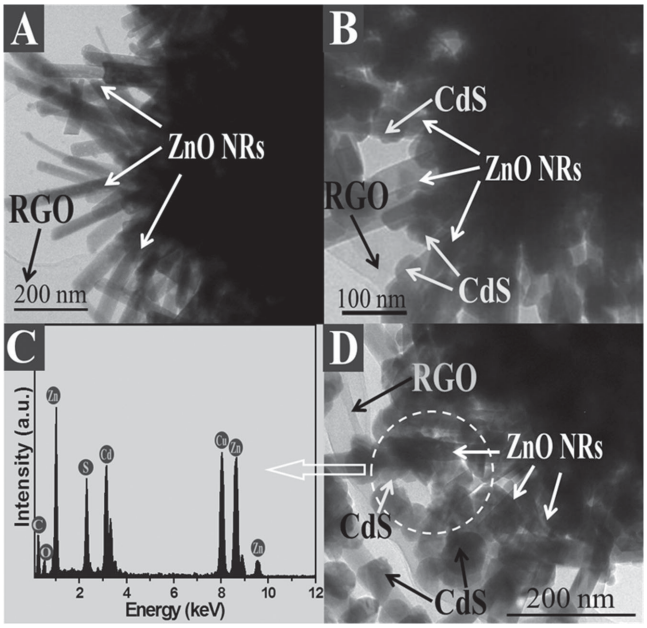


**Figure 3.** TEM images of A) 5%RGO-ZnO NRs, B, D) 5%RGO-ZnO NRs-CdS and C) the corresponding EDX spectrum for selected area of 5%RGO-ZnO NRs-CdS.

As shown in **Figure 6**A, under visible light irradiation, the photocurrent density for 5%RGO-ZnO NRs-CdS is much higher than that of ZnO nanostars-CdS and ZnO nanostars, suggesting a longer lifetime of charge carriers photogenerated over RGO-ZnO NRs-CdS than ZnO nanostars-CdS and ZnO nanostars,[3b,15b,16a] which qualitatively is in agreement with the results of photoluminescence (PL) spectra (Figure S9, Supporting Information). To further determine the advantage of 5%RGO-ZnO NRs-CdS over ZnO nanostars-CdS in improving the charge carriers transfer, electrochemical impedance spectra (EIS) Nyquist plots and cyclic voltammograms (CV), very useful tools to characterize the charge-carriers migration, have also been performed.[3c,16c] It can be seen from Figure 6B that 5%RGO-ZnO NRs-CdS shows smaller semicircle at high frequencies as compared to ZnO nanostars-CdS and ZnO nanostars, suggesting faster transport of charge carriers and more effective electron-hole pairs separation achieved over the 5%RGO-ZnO NRs-CdS electrode.[3c,16c] The cyclic voltammograms in Figure 6C show clear anodic and cathodic peaks for each sample. Since the preparation of the electrodes and electrolyte are identical for the CV curve measurement, the current density of the electrodes is related to the electron transfer rate of the electrode materials.[18] The current density obtained over the samples electrodes follows the order: 5%RGO-ZnO NRs-CdS > ZnO nanostars-CdS > ZnO nanostars, demonstrating that improved electron transfer is achieved over the ternary 5%RGO-ZnO NRs-CdS hybrid.[18] Controlled experiments (Figure S10, Supporting Information), using $K_2S_2O_8$ as scavenger for photogenerated electrons,[19] for reduction of 4-NA under visible light irradiation, confirm that the reduction reaction of aromatic nitro compounds is driven by the photogenerated electrons.[3c,16b,20]

The surface area and porosity of the samples have also been investigated. As shown in Figure S11 (Supporting Information), the nitrogen adsorption–desorption isotherm of ZnO nanostars exhibits type II isotherm according to the IUPAC classification, which along with the corresponding pore size distribution indicates the nonporous structure.[21] The ZnO nanostars-CdS and RGO-ZnO NRs-CdS hybrids have adsorption–desorption isotherms of type IV with a typical H3 hysteresis loop.[21] The BET surface areas of the samples are measured to be ca. 3, 5, 16, 22 and 26 $m^2 \cdot g^{-1}$ corresponding to ZnO nanostars, ZnO nanostars-CdS, 2%RGO-ZnO NRs-CdS, 5%RGO-ZnO NRs-CdS and 10%RGO-ZnO NRs-CdS, respectively (Table S1, Supporting Information). Obviously, the specific surface area of the samples is increased due to the introduction of RGO, particularly with the increase of weight addition ratios of RGO. The adsorption experiments performed in the dark for 4-NA (Figure S12, Supporting Information) reveal that the presence of RGO enhances the adsorptivity of RGO-ZnO NRs-CdS hybrids. Notably, although the 10%RGO-ZnO NRs-CdS possesses the largest specific surface area and adsorption capacity toward the reactant among the samples, its photoactivity is lower than that of 5%RGO-ZnO NRs-CdS. These results indicate that the primary factor accounting for the photoactivity enhancement of RGO-ZnO NRs-CdS nanocomposites cannot be ascribed to the

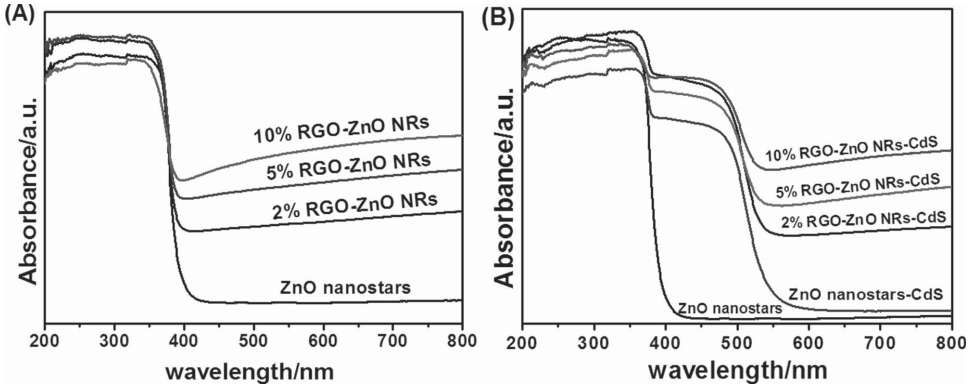


**Figure 4.** UV–Vis diffuse reflectance spectra (DRS) of the samples of A) blank ZnO nanostars, RGO-ZnO NRs with different weight addition ratios of RGO, B) blank ZnO nanostars, ZnO nanostars-CdS and RGO-ZnO NRs-CdS with different weight addition ratios of RGO.

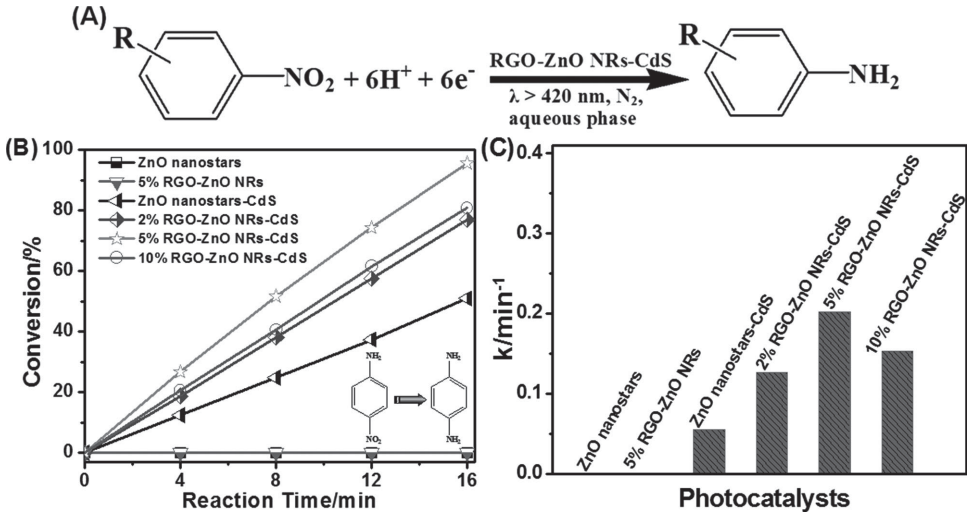


**Figure 5.** A) The formula for photocatalytic reduction of 4-NA to PPD, B) photocatalytic activities and C) apparent rate constants for selective reduction of 4-NA to PPD over bare ZnO nanostars, ZnO nanostars-CdS, 5%RGO-ZnO NRs and RGO-ZnO NRs-CdS with different weight addition ratios of RGO under visible light irradiation ($\lambda > 420$ nm).

differences in specific surface area and porosity of the samples, but to the improved charge carriers transport and synergistic interactions among RGO, semiconductor CdS and ZnO.

Based on the above discussions, it can be concluded that, in the hierarchical RGO-ZnO NRs-CdS hybrids, the 1D ZnO nanorod arrays are sensitized by the semiconductor CdS as visible light harvester and 2D RGO sheets act as co-catalyst to further promote the separation and transfer of photogenerated charge carriers from CdS upon visible light irradiation. The unique heterojunction structure and matched energy level position among CdS, ZnO and RGO are able to lead to the efficient three-level electron transfer for ternary RGO-ZnO NRs-CdS, as shown in **Figure 7**B, which is superior to two-level electron transfer of binary ZnO nanostars-CdS (Figure 7A).

Accordingly, a tentative reaction mechanism for photocatalytic selective reduction of aromatic nitro compounds to corresponding amino compounds over ternary RGO-ZnO NRs-CdS nanocomposites can be proposed, as illustrated in

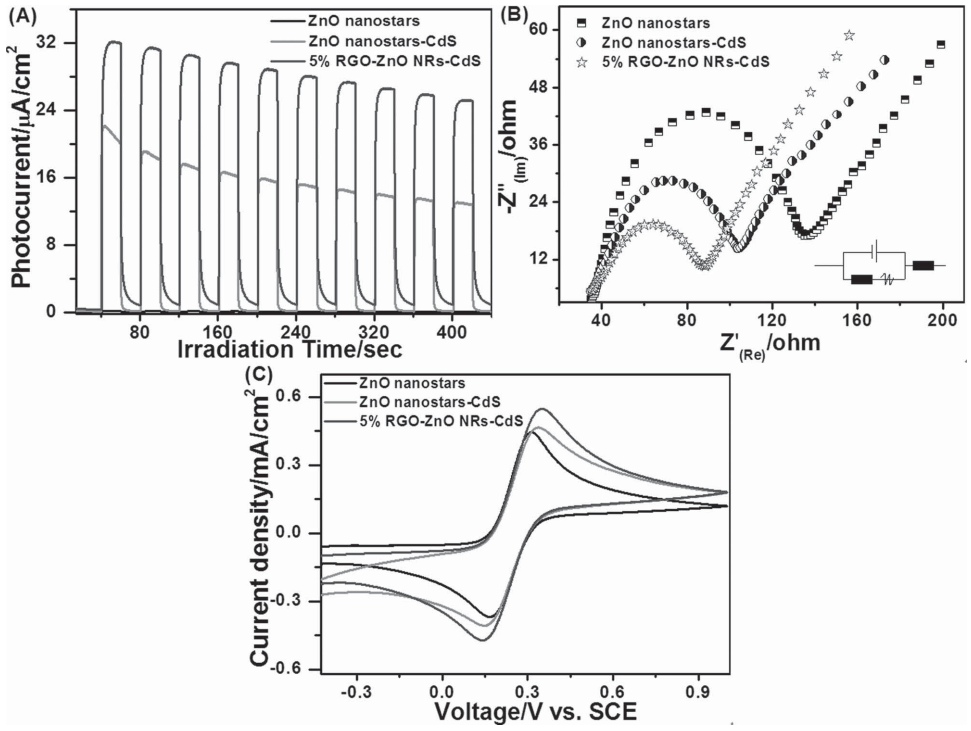


**Figure 6.** A) Transient photocurrent density, B) electrochemical impedance spectroscopy (EIS) Nyquist plots and C) cyclic voltammograms of the sample electrodes of ZnO nanostars, ZnO nanostars-CdS and 5%RGO-ZnO NRs-CdS.

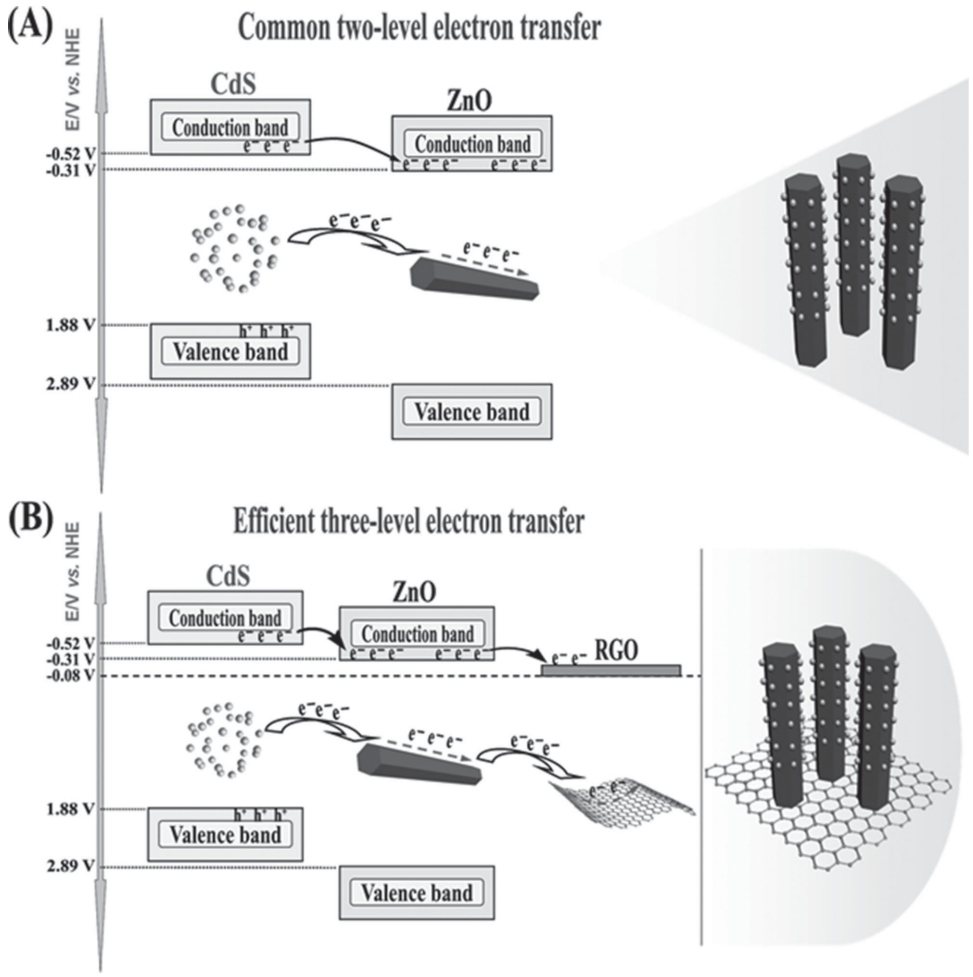


**Figure 7.** Schemes illustrating the transfer of charge carriers in A) binary ZnO nanostars-CdS nanocomposite and B) ternary RGO-ZnO NRs-CdS nanohybrids under visible light irradiation.

**Figure 8**. Under the illumination of visible light, CdS nanoparticles in the RGO-ZnO NRs-CdS photocatalysts are photoexcited to generate electron-hole pairs. On account of the more negative conduction band (CB) of CdS than that of ZnO nanorods, the electrons can easily transfer to the CB of ZnO from the CB of CdS. Subsequently, due to the introduction of RGO as an electron conductive platform, the work function of which is less negative than the CB of ZnO (–0.08 V for RGO vs NHE),[12,15a,20b,22] the photogenerated electrons can be injected to the RGO sheets. Such an efficient three-level electron transfer efficiently improves the fate and transfer of photogenerated electrons, thereby resulting in the enhanced photoreduction activity of the ternary RGO-ZnO NRs-CdS hybrids under visible light irradiation. Simultaneously, the photogenerated holes from CdS are trapped by the quenching agent of ammonium formate. In addition, the $N_2$ purge provides an anaerobic atmosphere for the reduction reaction. Meanwhile, the presence of RGO also increases the accumulating concentration of nitro compounds over the surface of RGO-ZnO NRs-CdS, which is also beneficial for improving the capability of the adsorbed aromatic nitro compounds to accept photogenerated electrons.

## 3. Conclusions

In summary, hierarchically CdS decorated 1D ZnO nanorods-2D graphene hybrids with ternary heteroassembly architectures have been successfully constructed via a convenient low-temperature heteroepitaxial growth strategy. In this architecture, the semiconductor CdS acts as photosensitizer for ZnO to capture visible light while 2D RGO sheets serve as co-catalyst to further promote the separation and transfer of photogenerated charge carriers from CdS upon visible light irradiation. Such a junction structure and matched energy level position among CdS, ZnO and RGO lead to the efficient three-level electron transfer for ternary RGO-ZnO NRs-CdS. Therefore, the ternary nanostructures exhibit markedly higher photocatalytic activity than the binary ZnO nanostars-CdS and blank ZnO nanostars under visible light illumination. In addition, the photocorrosion of ZnO and CdS is effectively inhibited by the control of reaction conditions, which involves the exclusion of formation of holes in ZnO by using visible light irradiation and the efficient consumption of holes photogenerated from CdS by the scavenger of ammonium formate, thereby resulting in the excellent photostability of the ternary hybrids toward selective photogenerated-electrons-driven reduction process. Our work provides a simple wet

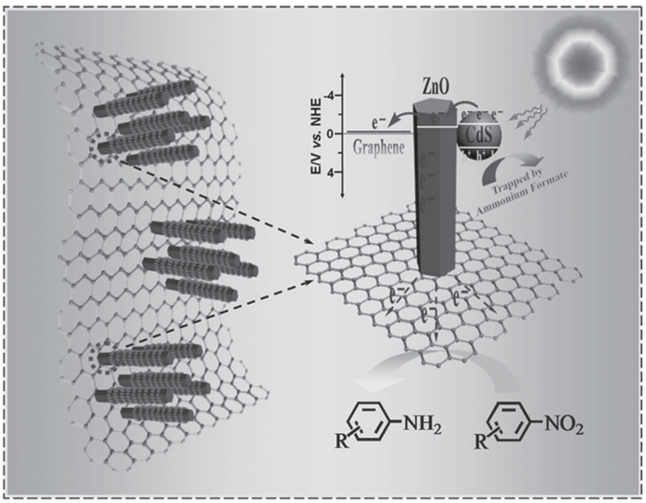


**Figure 8.** Illustration of the proposed reaction mechanism for photocatalytic reduction of nitro compounds in aqueous solution over the ternary RGO-ZnO NRs-CdS nanocomposites under visible light irradiation ($\lambda > 420$ nm).

chemical fabrication of hierarchical CdS-1D ZnO-2D graphene hybrids in pursuit of the desirable visible-light absorption of CdS and the electron conductive platform of 2D graphene as photosensitizer and co-catalyst respectively to widen the photocatalytic applications of ZnO by boosting charge carriers separation and transfer efficiency. Hopefully, this facile low temperature synthesis strategy could be extended to fabricating other hierarchical semiconductor-based heterogeneous assemblies to obtain novel unprecedented multifunctions and properties.

## 4. Experimental Section

*Materials*: All reagents were analytical grade and used without further purification., zinc acetate dehydrate ($C_4H_6O_4Zn{\cdot}2H_2O$), potassium hydroxide (KOH), zinc nitrate hexahydrate ($Zn(NO_3)_2{\cdot}6H_2O$), hexamethylenetetramine ($C_6H_{12}N_4$), thiourea ($NH_2CSNH_2$), ammonium formate ($HCOONH_4$), graphite powder, sulfuric acid ($H_2SO_4$), nitric acid ($HNO_3$), hydrochloric acid (HCl), potassium persulfate ($K_2S_2O_8$), phosphorus pentoxide ($P_2O_5$), hydrogen peroxide, 30% ($H_2O_2$), potassium permanganate ($KMnO_4$), methanol ($CH_4O$) and ethanol ($C_2H_6O$) were obtained from Sinopharm Chemical Reagent Co., Ltd. (Shanghai, China). Additionally, cadmium sulfate, 8/3-hydrate ($CdSO_4{\cdot}8/3H_2O$) was purchased from Aladdin. Deionized water used in the synthesis was from local sources.

*Preparation*: The unique graphene-ZnO nanorod arrays-CdS (RGO-ZnO NRs-CdS) nanohybrids, composed of CdS deposition onto the hedgehog-like graphene-ZnO nanorod arrays (RGO-ZnO NRs), have been fabricated by a facile and efficient two-step refluxing method, as illustrated in Scheme 1. *(I) Fabrication of ZnO seeds.* ZnO sol–gel solution was prepared as reported previously.[23] 125 mL zinc acetate dehydrate solution in methanol (0.01 M) was prepared under vigorous stirring at 60 °C. Then, 65 mL KOH solution in methanol (0.03 M) was injected dropwise into the above solution. The sol–gel solution of ZnO seeds was obtained for the following reaction after continuous stirring at 60 °C for 2 h. *(II) Synthesis of star-like ZnO nanorods (ZnO nanostars).* 50 mL solution of ZnO seeds was centrifuged and washed with anhydrous ethanol. The obtained white precipitate was well dispersed by sonication in 150 mL aqueous solution containing $Zn(NO_3)_2$ (0.02 M) and $C_6H_{12}N_4$ (HMT, 0.02 M). After vigorous stirring, the mixed solution was refluxed at 95 °C for 6 h. ZnO nanostars were obtained after filtration and drying process. *(III) Synthesis of ZnO nanostars-CdS nanocomposite.* 0.05 g as-prepared ZnO nanostars were redispersed via the assist of ultrasonication in 130 mL deionized water to obtain the homogeneous suspension. Then 0.2 mmol $CdSO_4{\cdot}8/3H_2O$ and 0.4 mmol $NH_2CSNH_2$ were added into the above suspension under vigorous stirring for 30 min. After the refluxing process at 95 °C for 3 h, the products were cooled to room temperature and recovered by filtration, washed by water, and fully dried at 60 °C in an oven to obtain the ZnO nanostars-CdS nanocomposite. *(IV) Synthesis of RGO-ZnO NRs-CdS nanocomposites by a seed-assisted assembly strategy.* GO was synthesized from natural graphite powder by a modified Hummers method, which was also used in our previous studies.[1d,3b,9a,15a,16c,19,20b,24] The detail for fabricating GO is presented in the Supporting Information. GO was well dispersed in methanol by assist of ultrasonication and then mixed with the as-prepared ZnO seeds solution. After 2 h stirring, the suspension was centrifuged at 2500 rpm followed by washing with ethanol twice. Subsequently, the obtained ZnO seed-coated GO sheets suspension was dispersed by sonication in 150 mL aqueous solution containing $Zn(NO_3)_2$ (0.02 M) and $C_6H_{12}N_4$ (HMT, 0.02 M). After vigorous stirring, the mixed solution was refluxed at 95 °C for 6 h to achieve heteroepitaxial growth of ZnO nanorods onto the graphene substrate. The products were cooled to room temperature, centrifuged and washed for three times to obtain the hedgehog-like RGO-ZnO NRs with different weight addition ratios of RGO, namely, 2, 5, and 10% nanocomposites. The RGO-ZnO NRs-CdS nanocomposites were prepared via the same synthetic procedures of ZnO nanostars-CdS just using RGO-ZnO NRs nanocomposites instead of ZnO nanostars. Thus, after the CdS decoration, the RGO-ZnO NRs-CdS nanocomposites with different weight addition ratios of RGO (i.e., 2RGO-ZnO NRs-CdS, 5RGO-ZnO NRs-CdS, 10RGO-ZnO NRs-CdS) were obtained.

*Characterization*: The crystal phase properties of the samples were analyzed with a Bruker D8 Advance X-ray diffractometer (XRD) using Ni-filtered Cu K$\alpha$ radiation at 40 kV and 40 mA in the 2$\theta$, ranging from 5° to 80° with a scan rate of 0.02° per second. Field-emission scanning electron microscopy (FESEM) was used to determine the morphology of the samples on a FEI Nova NANOSEM 230 spectrophotometer. Transmission electron microscopy (TEM) images were obtained using a JEOL model JEM 2010 EX instrument at an accelerating voltage of 200 kV. X-ray photoelectron spectroscopy (XPS) measurements were carried out on a Thermo Scientific ESCA Lab250 spectrometer which consists of a monochromatic Al K$\alpha$ as the X-ray source, a hemispherical analyzer and sample stage with multi-axial adjustability to obtain the surface composition of the sample. All of the binding energies were calibrated by the C 1s peak at 284.6 eV. The details of XPS fitting are as follows: choosing Smart subtraction for the peak background subtraction and Gaussian shape as the shape of the peaks used for the deconvolution. Raman spectroscopic measurements were performed on a Renishaw inVia Raman System 1000 with a 532 nm Nd:YAG excitation source at room temperature. The optical properties of the samples were analyzed by UV–Vis diffuse reflectance spectroscopy (DRS) using a UV–Vis spectrophotometer (Cary-500, Varian Co.), in which $BaSO_4$ was used as the internal reflectance standard. The electrochemical analysis was carried out in a conventional three-electrode cell using a Pt plate and an Ag/AgCl electrode as the counter electrode and reference electrode, respectively. The electrolyte was 0.2 M $Na_2SO_4$ aqueous solution without additive (pH = 6.8). The working electrode was prepared on indium-tin oxide (ITO) glass which was cleaned by sonication in ethanol for 30 min and dried at 353 K. The boundary of ITO glass was protected using scotch tape. 5 mg sample was dispersed in 0.5 mL N,N-Dimethylflormamide (DMF, supplied from Sinopharm Chemical Reagent Co., Ltd.) by sonication to get slurry. The slurry was spread onto the pretreated ITO glass. After air drying, the working electrode was further dried at 393 K for 2 hours to improve adhesion. Then the scotch tape was unstuck and the uncoated part of the electrode was isolated with epoxy resin. The exposed area of the working electrode was 0.25 $cm^2$. The photocurrent measurements were taken on a BAS Epsilon workstation without bias. The electrochemical impedance spectroscopy (EIS) measurements were performed via an EIS spectrometer (CHI-660D workstation, CH Instruments) in a three-electrode cell in the presence of 5.0 mM $K_3[Fe(CN)_6]/K_4[Fe(CN)_6]$ by applying an AC voltage with 5 mV amplitude in a frequency range from 1 Hz to 100 kHz

under open circuit potential conditions. The cyclic voltammograms were measured in 0.5 M KCl solution containing 10.0 mM $K_3[Fe(CN)_6]$/$K_4[Fe(CN)_6]$ as a redox probe with the scanning rate of 20 mV/s in the same three-electrode cell as EIS measurement. The photoluminescence (PL) spectra for solid samples were investigated on an Edinburgh FL/FS900 spectrophotometer with an excitation wavelength of 370 nm.

*Photocatalytic Activity*: In a typical photocatalytic reaction, a 300 W Xe arc lamp (PLS-SXE 300, Beijing Perfect light Co., Ltd.) with a UV–CUT filter to cut off light of wavelength $\lambda < 420$ nm was used as the irradiation source. 10 mg of the samples and 40 mg $HCOONH_4$ (hole scavenger) were added into 40 mL of the aromatic nitro compounds solution (10 mg·$L^{-1}$) in a quartz vial. Before visible light illumination, the above suspension was stirred in the dark for 1 h to ensure the establishment of adsorption–desorption equilibrium between the sample and reactant. During the process of the reaction, 3 mL of sample solution was collected at a certain time interval and centrifuged to remove the catalyst completely at 12000 rmp. Afterward, the solution was analyzed on a Varian ultraviolet-visible light (UV–Vis) spectrophotometer (Cary-50, Varian Co.). The whole experimental process was conducted under $N_2$ bubbling at the flow rate of 80 mL·$min^{-1}$.

## Supporting Information

Supporting Information is available from the Wiley Online Library or from the author.

## Acknowledgements

The support by the National Natural Science Foundation of China (NSFC) (20903023, 21173045), the Award Program for Minjiang Scholar Professorship, the Natural Science Foundation (NSF) of Fujian Province for Distinguished Young Investigator Grant (2012J06003), Program for Returned High-Level Overseas Chinese Scholars of Fujian province, and the Project sponsored by the Scientific Research Foundation for the Returned Overseas Chinese Scholars, State Education Ministry, is gratefully acknowledged.

Received: July 22, 2014
Revised: September 1, 2014
Published online: October 13, 2014

[1] a) X. Chen, S. S. Mao, *Chem. Rev.* **2007**, *107*, 2891–2959; b) Y.-F. Li, Z.-P. Liu, *J. Am. Chem. Soc.* **2011**, *133*, 15743–15752; c) S. Yurdakal, G. Palmisano, V. Loddo, V. Augugliaro, L. Palmisano, *J. Am. Chem. Soc.* **2008**, *130*, 1568–1569; d) Y. Zhang, Z.-R. Tang, X. Fu, Y.-J. Xu, *ACS Nano* **2010**, *4*, 7303–7314; e) Y. Zhang, N. Zhang, Z.-R. Tang, Y.-J. Xu, *Chem. Sci.* **2012**, *3*, 2812–2822; f) N. Zhang, R. Ciriminna, M. Pagliaro, Y.-J. Xu, *Chem. Soc. Rev.* **2014**, *43*, 5276–5287; g) J. C. Colmenares, R. Luque, *Chem. Soc. Rev.* **2014**, *43*, 765–778; h) J. C. Colmenares, *ChemSusChem* **2014**, *7*, 1512–1527.

[2] a) H. G. Yang, C. H. Sun, S. Z. Qiao, J. Zou, G. Liu, S. C. Smith, H. M. Cheng, G. Q. Lu, *Nature* **2008**, *453*, 638–641; b) F. Zaera, *J. Phys. Chem. Lett.* **2010**, *1*, 621–627; c) H. C. Zeng, *Acc. Chem. Res.* **2013**, *46*, 226–235; d) K. Zhou, Y. Li, *Angew. Chem. Int. Ed.* **2012**, *51*, 602–613.

[3] a) Y. Mao, S. S. Wong, *J. Am. Chem. Soc.* **2006**, *128*, 8217–8226; b) Y. Zhang, Z.-R. Tang, X. Fu, Y.-J. Xu, *ACS Nano* **2011**, *5*, 7426–7435; c) Y. Zhang, N. Zhang, Z.-R. Tang, Y.-J. Xu, *ACS Sustainable Chem. Eng.* **2013**, *1*, 1258–1266.

[4] a) Z.-R. Tang, F. Li, Y. Zhang, X. Fu, Y.-J. Xu, *J. Phys. Chem. C* **2011**, *115*, 7880–7886; b) F. Xiao, *J. Phys. Chem. C* **2012**, *116*, 16487–16498; c) J.-Y. Liao, B.-X. Lei, H.-Y. Chen, D.-B. Kuang, C.-Y. Su, *Energy Environ. Sci.* **2012**, *5*, 5750–5757; d) W. Guo, C. Xu, X. Wang, S. Wang, C. Pan, C. Lin, Z. L. Wang, *J. Am. Chem. Soc.* **2012**, *134*, 4437–4441; e) H. Huang, L. Pan, C. K. Lim, H. Gong, J. Guo, M. S. Tse, O. K. Tan, *Small* **2013**, *9*, 3153–3160.

[5] a) Z. L. Wang, J. Song, *Science* **2006**, *312*, 242–246; b) H. Yu, Z. Zhang, M. Han, X. Hao, F. Zhu, *J. Am. Chem. Soc.* **2005**, *127*, 2378–2379; c) L. Vayssieres, *Adv. Mater.* **2003**, *15*, 464–466; d) L. L. Yang, Q. X. Zhao, M. Willander, X. J. Liu, M. Fahlman, J. H. Yang, *Cryst. Growth Des.* **2010**, *10*, 1904–1910; e) C. Ren, B. Yang, M. Wu, J. Xu, Z. Fu, Y. lv, T. Guo, Y. Zhao, C. Zhu, *J. Hazard. Mater.* **2010**, *182*, 123–129; f) S. Xu, Y. Qin, C. Xu, Y. Wei, R. Yang, Z. L. Wang, *Nat. Nanotechnol.* **2010**, *5*, 366–373.

[6] a) Y. Tak, S. J. Hong, J. S. Lee, K. Yong, *J. Mater. Chem.* **2009**, *19*, 5945–5951; b) Y. Wei, W. Wu, R. Guo, D. Yuan, S. Das, Z. L. Wang, *Nano Lett.* **2010**, *10*, 3414–3419; c) C. Geng, Y. Jiang, Y. Yao, X. Meng, J. A. Zapien, C. S. Lee, Y. Lifshitz, S. T. Lee, *Adv. Funct. Mater.* **2004**, *14*, 589–594; d) X. Wang, C. J. Summers, Z. L. Wang, *Nano Lett.* **2004**, *4*, 423–426.

[7] a) N. Zhang, Y. Zhang, Y.-J. Xu, *Nanoscale* **2012**, *4*, 5792–5813; b) W. Tu, Y. Zhou, Z. Zou, *Adv. Funct. Mater.* **2013**, *23*, 4996–5008; c) Y. Zhu, S. Murali, W. Cai, X. Li, J. W. Suk, J. R. Potts, R. S. Ruoff, *Adv. Mater.* **2010**, *22*, 3906–3924; d) G. Xie, K. Zhang, B. Guo, Q. Liu, L. Fang, J. R. Gong, *Adv. Mater.* **2013**, *25*, 3820–3839; (e) M.-Q. Yang, N. Zhang, M. Pagliaro, Y.-J. Xu, *Chem. Soc. Rev.* **2014**, DOI: 10.1039/c4cs00213j.

[8] X. Wang, G. Liu, Z.-G. Chen, F. Li, L. Wang, G. Q. Lu, H.-M. Cheng, *Chem. Commun.* **2009**, 3452–3454.

[9] a) B. Weng, M.-Q. Yang, N. Zhang, Y.-J. Xu, *J. Mater. Chem. A* **2014**, *2*, 9380–9389; b) Z. B. Yu, Y. P. Xie, G. Liu, G. Q. Lu, X. L. Ma, H.-M. Cheng, *J. Mater. Chem. A* **2013**, *1*, 2773–2776; c) C. Han, M.-Q. Yang, B. Weng, Y.-J. Xu, *Phys. Chem. Chem. Phys.* **2014**, *16*, 16891–16903.

[10] a) Y. Yang, L. Qu, L. Dai, T. S. Kang, M. Durstock, *Adv. Mater.* **2007**, *19*, 1239–1243; b) L. Yang, Y. Zhang, W. Ruan, B. Zhao, W. Xu, J. R. Lombardi, *J. Raman Spectrosc.* **2010**, *41*, 721–726.

[11] K. Pan, Y. Dong, W. Zhou, Q. Pan, Y. Xie, T. Xie, G. Tian, G. Wang, *ACS Appl. Mater. Interfaces* **2013**, *5*, 8314–8320.

[12] M.-Q. Yang, Y.-J. Xu, *Phys. Chem. Chem. Phys.* **2013**, *15*, 19102–19118.

[13] Y. T. Liang, B. K. Vijayan, K. A. Gray, M. C. Hersam, *Nano Lett.* **2011**, *11*, 2865–2870.

[14] S. Sahoo, A. K. Arora, *J. Phys. Chem. B* **2010**, *114*, 4199–4203.

[15] a) N. Zhang, Y. Zhang, M.-Q. Yang, Z.-R. Tang, Y.-J. Xu, *J. Catal.* **2013**, *299*, 210–221; b) Q. Xiang, J. Yu, M. Jaroniec, *J. Am. Chem. Soc.* **2012**, *134*, 6575–6578.

[16] a) N. Zhang, Y.-J. Xu, *Chem. Mater.* **2013**, *25*, 1979–1988; b) F.-X. Xiao, J. Miao, B. Liu, *J. Am. Chem. Soc.* **2014**, *136*, 1559–1569; c) N. Zhang, M.-Q. Yang, Z.-R. Tang, Y.-J. Xu, *ACS Nano* **2014**, *8*, 623–633.

[17] A. Primo, T. Marino, A. Corma, R. Molinari, H. García, *J. Am. Chem. Soc.* **2011**, *133*, 6930–6933.

[18] a) M. Jahan, Z. Liu, K. P. Loh, *Adv. Funct. Mater.* **2013**, *23*, 5363–5372; b) X. Pan, Y. Zhao, S. Liu, C. L. Korzeniewski, S. Wang, Z. Fan, *ACS Appl. Mater. Interfaces* **2012**, *4*, 3944–3950.

[19] Y. Zhang, Z. Chen, S. Liu, Y.-J. Xu, *Appl. Catal., B* **2013**, *140–141*, 598–607.

[20] a) B. Weng, S. Liu, N. Zhang, Z.-R. Tang, Y.-J. Xu, *J. Catal.* **2014**, *309*, 146–155; b) M.-Q. Yang, B. Weng, Y.-J. Xu, *Langmuir* **2013**, *29*, 10549–10558; c) F.-X. Xiao, J. Miao, H. Yang, J. Chen, B. Liu, *Nanoscale* **2014**, *6*, 6727–6737.

[21] K. S. W. Sing, D. H. Everett, R. A. W. Haul, L. Moscou, R. A. Pierotti, J. Rouquérol, T. Siemieniewska, *Pure Appl. Chem.* **1985**, *57*, 603–619.

[22] J. Zhang, J. Yu, M. Jaroniec, J. R. Gong, *Nano Lett.* **2012**, *12*, 4584–4589.

[23] a) C. Pacholski, A. Kornowski, H. Weller, *Angew. Chem. Int. Ed.* **2002**, *41*, 1188–1191; b) S. Wang, Y. Yu, Y. Zuo, C. Li, J. Yang, C. Lu, *Nanoscale* **2012**, *4*, 5895–5901.

[24] X. Pan, M.-Q. Yang, Y.-J. Xu, *Phys. Chem. Chem. Phys.* **2014**, *16*, 5589–5599.